

Multigeophysical Inversion for Geothermal Exploration

Ketil Hokstad¹ and Claudia Kruber²

¹Equinor Research Centre, Trondheim, Norway, ²Equinor Bergen, Norway.

Keywords

Geophysics, rock physics, Bayesian inversion, temperature, porosity, exploration, IDDP

ABSTRACT

A method for multigeophysical inversion for geothermal systems is presented. Datasets and models input to the inversion may include one or more of the following geophysical parameters: resistivity, magnetization, density and seismic P-wave and S-wave velocities, or v_p/v_s -ratio. Rock physics models relating geophysical parameters to temperature and porosity are needed as part of the inversion and have been developed as part of the work presented.

The proposed method is based on a naïve Bayes network, such that posterior mean and variance of temperature and porosity of geothermal systems can be estimated. The multigeophysical inversion can be used as part of a 3D geothermal play-fairway analysis. It may contribute to the derisking of the heat source, recharge and producibility play elements.

The proposed multigeophysical inversion is demonstrated on field data from the Hengill geothermal area on Iceland, with the purpose of contributing to exploration and siting of the IDDP-3 well.

1. Introduction

Wells targeting supercritical and superhot geothermal systems may significantly increase the energy output from geothermal wells. It is estimated that the energy output may be increased by a factor of 5-10 compared to a conventional geothermal system (Fridleifsson et al., 2014, Okamoto et al., 2019). Supercritical geothermal systems will usually be blind systems, masked by a conventional system above. Hence, the challenges related to exploration for supercritical systems will be significant.

The petroleum-system analysis developed by the petroleum industry has been adapted to geothermal systems. It is commonly known as play fairway analysis (PFA). Geothermal PFA for conventional geothermal resources, using a 2D mapping approach (Faulds et al., 2018), has been demonstrated in a number of projects supported by the US Department of Energy. An extension of the PFA concept to target supercritical systems may require a 3D PFA approach, as suggested by Kolker et al. (2022).

A major task to be performed in PFA, is the integration of various types of geophysical, geological and geochemical datasets, in order to derisk the play elements of a geothermal play. In this paper, a methodology is presented for multigeophysical inversion (MGI) of electromagnetic data, seismic data and potential field data. MGI may contribute to derisking of the heat source, recharge and producibility play elements, and may be used as part of a 3D PFA workflow.

The Iceland Deep Drilling Project (IDDP) is a long-term scientific effort, with the ultimate goal of producing geothermal energy from fluids in the temperature range 400-600 °C, or enthalpy of order 3000 kJ/kg (Friðleifsson, et al., 2014). The IDDP-1 well was drilled near the Krafla volcano, and encountered rhyolitic magma at 2.1 km depth (Elders et al., 2011). The IDDP-2 well was drilled at Reykjanes, and reached a depth of 4600m, and temperatures close to 600 °C (Friðleifsson et al., 2018; Bali et al., 2022). The third and last IDDP well, IDDP-3, is planned to be drilled in the Hengill geothermal area, operated by Reykjavik Energy (OR).

The work presented here is part of the multinational research project “Derisking Exploration for Multiple Geothermal Plays in Magmatic Environments” (DEEPEN). The DEEPEN project focus on tools and methods for detection of supercritical targets (Hjorleifsdottir et al, 2023). One of the goals of the DEEPEN project is to contribute to the siting of the IDDP-3 well.

2. Naïve-Bayes network for multigeophysical inversion

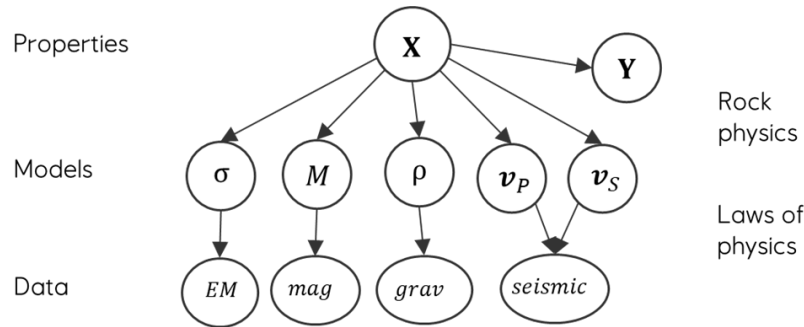


Figure 1: Bayesian network representing geophysical data, geophysical models, and properties of interest. σ is electric conductivity, M is magnetization, ρ is density, v_p is seismic P-wave velocity, and v_s is seismic S-wave velocity. X represents properties of interest, temperature and porosity in the geothermal case, and Y may represent geological and geochemical information.

Multigeophysical inversion based on Bayesian networks (Figure 1) has proven to be a useful tool for quantitative integration of multiple geophysical datasets. MGI has previously been developed for a variety of applications, including basin modeling (Hokstad et al., 2017), geothermal exploration (Hokstad and Tānavsuu-Milkeviciene, 2017), petroleum-reservoir characterization (Miotti et al., 2020), and marine mineral exploration (Hokstad, 2020, 2022).

The naïve-Bayes structure of the network (Figure 1) occurs when the geophysical data and geophysical models are conditionally independent. This is the case if the noise in the various geophysical datasets is independent, which is a reasonable assumption (e.g. the noise in seismic data acquired in 2020 is independent of the noise in magnetic data measured in 2016). Then geophysical models can be obtained by single-domain inversions of each geophysical dataset. Subsequently, properties of interest may be computed by combination of geophysical models.

The relationship between geophysical models and geophysical data are governed by the laws of physics (the Maxwell equations, magnetostatic equation, elastic wave equation, and Newton's law of gravity). Geophysical model parameters are related to properties of interest by rock-physics equations. For geothermal exploration, the properties of interest are temperature and porosity. Permeability cannot be estimated directly from geophysical data, but can, eventually, be obtained via porosity-permeability relationships (Mavko et al., 2009, Ch. 8.4).

In application of MGI, we often take a pragmatic approach, such that geophysical models from single-domain inversions, performed by various geoscientists and service providers, can be utilized. Therefore, we focus the Bayesian inversion on the second stage of the inversion, computing subsurface temperature and porosity from 3D geophysical models. This becomes effectively a Bayesian rock-physics inversion.

For the geothermal variety of the naïve-Bayes network, the posterior probability for temperature and porosity can be written as

$$p(T, \phi | m_1, \dots, m_n) = c \prod_{i=1}^n p(m_i | T, \phi) p(T, \phi), \quad (1)$$

where T is temperature, ϕ is porosity, m_i are the geophysical model parameters, and c is the normalization factor. The prior distribution for temperature and porosity is denoted $p(T, \phi)$. Assuming Gaussian noise, the likelihood distribution for each geophysical parameter, can be written as

$$p(m_i | T, \phi) = \frac{1}{|2\pi\Sigma_{ei}|^{\frac{1}{2}}} e^{-[m_i - F_i(T, \phi)]^T \Sigma_{ei}^{-1} [m_i - F_i(T, \phi)]}, \quad (2)$$

where $F_i(T, \phi)$ is the rock-physics relation for the dependence of model parameter m_i on temperature and porosity, and Σ_{ei} is the corresponding noise covariance. Geophysical model parameters m_i may include electric conductivity σ (or resistivity $R_h = 1/\sigma$), magnetization M , density ρ , seismic P-wave velocity v_p , S-wave velocity v_s , or alternatively the v_p/v_s -ratio. Geological and geochemical information can in principle also be included, however, a proper combination of information in the form of cubes, maps and point datasets is often a challenge.

When the posterior distribution $p(T, \phi | m_1, \dots, m_n)$ is known, the posterior mean, variance and covariance of temperature and porosity can be computed from the definitions. Inversion for temperature only can be achieved by setting the prior variance of porosity to a tiny value, thereby locking the porosity to the prior value. Inversion for porosity only can be performed correspondingly, by locking the temperature to the prior value.

2. Rock-physics equations

To be useful in the likelihood distributions in Equation 2, rock-physics models with an explicit dependence on temperature and porosity are needed. In this section, rock physics equations for electric conductivity, magnetization, density, P-wave velocity and S-wave velocity are presented.

The rock-physics models will usually require local calibration to each location and case considered. This is also the case when rock-physics is applied in petroleum-related problems, where models often need to be calibrated per geological formation (Avseth and Lehocki, 2021).

In the equations below, the unit of temperature is Kelvin (K), though for convenience, plots are mostly displayed with degrees Celsius as temperature axis.

2.1 Electric conductivity

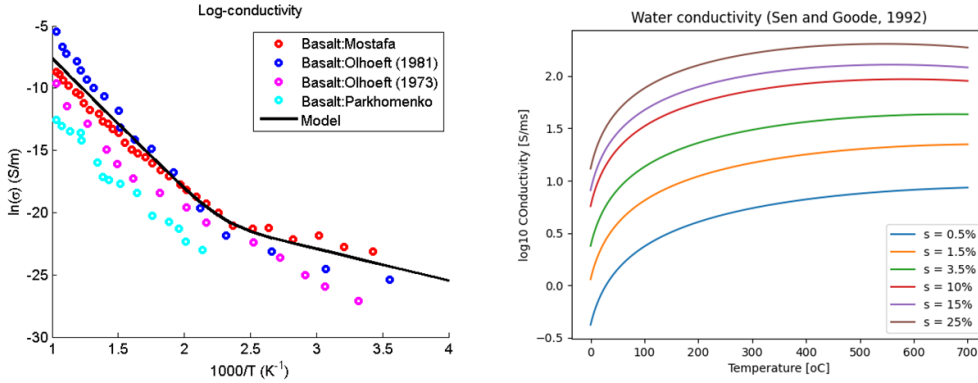


Figure 2: Temperature-dependent conductivity of basalt rock matrix (left) and saline water (right).

The electric conductivity is modeled as a parallel coupling of conductors, representing rock matrix (basalt/gabbro), clay, and pore space filled with brine,

$$\sigma = (1 - \phi - V_{cl}) \sigma_m + \phi \sigma_a + V_{cl} \sigma_{cl}. \quad (3)$$

Here σ_m is temperature-dependent matrix conductivity, σ_{cl} is clay conductivity, σ_a is conductivity of pore-space filled with brine (Archie's law), ϕ is porosity, and V_{cl} is clay fraction. The corresponding electric resistivity is given by $R_h = 1/\sigma$. The temperature-dependent matrix conductivity, with two conduction mechanisms (Figure 2), can be written as (Mostafa et al., 2003; Hokstad and Tănăvsu-Milkeviciene, 2017),

$$\sigma_m(T) = \sigma_1 e^{-\frac{E_1}{k_B T}} + \sigma_2 e^{-\frac{E_2}{k_B T}}, \quad (4)$$

where k_B is the Boltzmann constant, and σ_j and E_j (for $j=1,2$) are calibration parameters. E_j play the role of activation energies for two temperature-dependent conduction mechanisms. The conductivity of brine-filled porosity is modeled using the Archie equation (Mavko et al., 2009, Ch. 9.4) and the fracture-porosity model, presented by Brace and Orange (1968),

$$\sigma_a(T) = a_0 \phi \sigma_w(T, s). \quad (5)$$

The conductivity of water σ_w depends on temperature and salinity (Figure 2), as given by Sen and Goode (1992),

$$\sigma_w(T, s) = m[5.6 + 0.27(T - T_0) - 1.5 \cdot 10^{-4}(T - T_0)^2] - \frac{m^{3/2}[2.36 + 0.099(T - T_0)]}{1 + 0.214m}, \quad (6)$$

where s is salinity, $m = s/0.05844$ is the molality of salt and $T_0 = 273K$. The clay (smectite) conductivity due to cation exchange is modeled by the Waxman-Smiths equation (Mavko et al., 2009, Ch. 9.4),

$$\sigma_{cl}(T) = \phi(1 - \phi)CB, \quad (7)$$

$$B = 4.6 \left[1 - 0.6e^{-\frac{\sigma_w(t)}{1.3}} \right], \quad (8)$$

where C is the cation-exchange capacity (meq/100g), and ρ_{cl} is the clay-mineral density.

2.2 Seismic P-wave velocity, S-wave velocity and density

The rock-physics models for density, P-wave velocity and S-wave velocity must be considered together, since the temperature dependence is described for density, bulk modulus and shear modulus. The temperature dependence of the matrix properties is mainly due to volume expansion. The relationship between expansivity and temperature T can be expressed as (Hacker et al., 2003)

$$\alpha(T) = a_0 \left(1 - \frac{10}{\sqrt{T}} \right), \quad (9)$$

$$\Phi = \int_{T_0}^T \alpha(T')dT' = a_0[(T - T_0) - 20(\sqrt{T} - \sqrt{T_0})]. \quad (10)$$

Then the temperature-dependent matrix density $\rho_m(T)$ can be written as

$$\rho_m(T) = \rho_0 e^{-\Phi}, \quad (11)$$

where ρ_0 is the density at temperature T_0 . The temperature dependence of the matrix bulk and shear moduli $K_m(T)$ and $\mu_m(T)$ are correspondingly given by

$$K_m(T) = K_0 e^{-\delta_T \Phi}, \quad (12)$$

$$\mu_m(T) = \mu_0 e^{-\Gamma_T \Phi}, \quad (13)$$

where K_0 and μ_0 are the bulk and shear moduli at $T = T_0$, and δ_T and Γ_T are the Grüneisen parameters (Hacker et al., 2003). The temperature-dependent seismic P- and S-wave velocities of the rock matrix are then given by

$$v_{Pm}(T) = \sqrt{\frac{K_m(T) + (4/3)\mu_m(T)}{\rho_m(T)}}, \quad (14)$$

$$v_{Sm}(T) = \sqrt{\frac{\mu_m(T)}{\rho_m(T)}}. \quad (15)$$

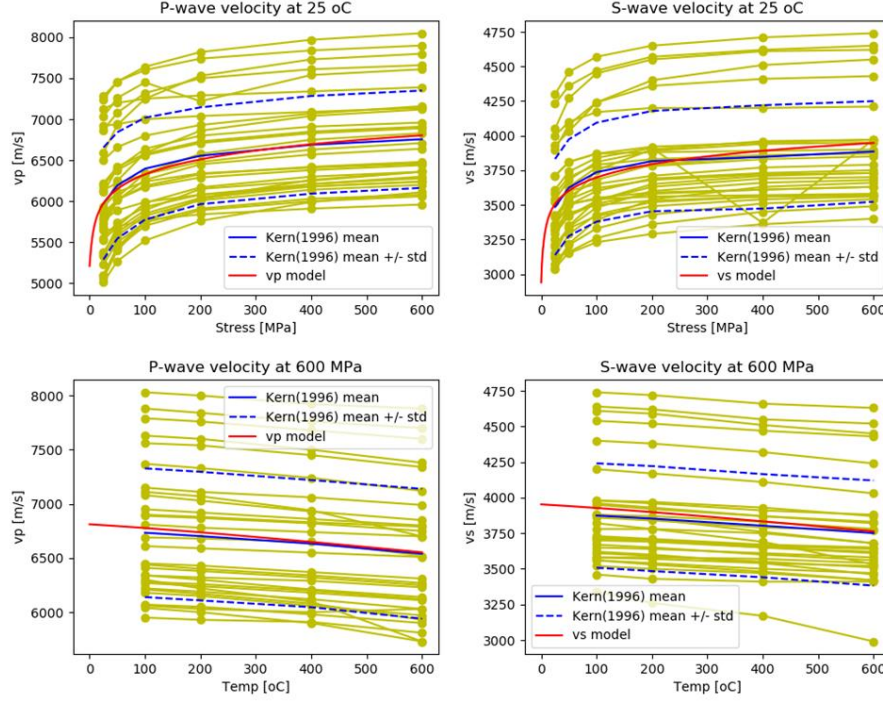


Figure 3: Temperature and effective stress dependence of seismic P-wave and S-wave velocities. Comparison of the model presented in Equations 16 and 17, (red lines) and the experimental data of Kern et al. (1996).

To account for the effects of porosity ϕ and clay fraction V_{cl} on the seismic velocities, we use a linearized model as suggested by Han (1986). The effective-stress dependence is modeled as proposed by Eberhardt-Phillips et al. (1889),

$$v_P(T, \phi, V_{cl}, \sigma') = v_{P_m}(T) - A_P \phi - B_P V_{cl} + C_P (\sigma' - D_P e^{-\beta \sigma'}), \quad (16)$$

$$v_S(T, \phi, V_{cl}, \sigma') = v_{S_m}(T) - A_S \phi - B_S V_{cl} + C_S (\sigma' - D_S e^{-\beta \sigma'}), \quad (17)$$

where $A_\eta, B_\eta, C_\eta, D_\eta$ are empirical coefficients (for $\eta = \{P, S\}$). The effective stress σ' is the lithostatic stress, carried by the rock matrix, minus the pressure of the pore fluids P ,

$$\sigma' = \sigma - P. \quad (18)$$

In the hydrostatic case, the effective stress is given by

$$\sigma'(z) = \int_0^z g_z [\rho(z', T, \phi, V_{cl}) - \rho_w(T, s)] dz', \quad (19)$$

where g_z is the acceleration of gravity, and ρ_w is the temperature- and salinity-dependent density of water. The bulk density is then be written as

$$\rho(T, \phi, V_{cl}) = (1 - \phi - V_{cl}) \rho_m(T) + V_{cl} \rho_{cl} + \phi \rho_w(T, s). \quad (20)$$

where ρ_{cl} is the clay density.

The temperature and effective-stress dependence of the seismic velocities are in qualitative agreement with the experimental work of Kern et al. (1996). Porosity is a first-order effect on

seismic velocities, and the effective-stress will usually give a larger contribution than temperature (Figure 3). The spread in the experimental results of Kern et al. (1996) may be explained by variations in porosity.

2.3 Magnetization

The main carrier of magnetization in basaltic, oceanic crust is iron-titanium oxides. The initial magnetic mineral is titanomagnetite, with chemical formula $Fe_{3-u}Ti_uO_4$, belonging to the spinel group. The titanomagnetites in fresh oceanic crust exhibits a rather uniform composition, with 60% ulvöspinel ($u=0.6$) and 40% magnetite, often referred to as TM60 (Butler, 1992; Pariso and Johnson, 1991). The volume fraction of iron-titanium oxides in basaltic rocks is typically $\sim 5\%$ (Butler, 1992). When lava cools and solidifies, significant changes of magnetic properties may take place. Processes with major influence on the magnetization of basalts are:

1. High temperature oxidation (Butler, 1992)
2. Low temperature hydrothermal oxidation (Ade-Hall et al., 1971; Prevot et al., 1981, Gapeev and Gribov, 1990; Zhou et al., 2001; Oliva-Urcia et al., 2011)
3. Solid exsolution (Yund and McAllister, 1969; Wise et al., 2011; Hokstad et al., 2020)

The Curie (Neel) temperature is the critical temperature for ferromagnetism (antiferromagnetism). Near the Curie temperature, materials lose their permanent magnetization, and become paramagnetic. Laboratory measurements on rock samples from the Hellisheiði geothermal field on Iceland shows that 2 to 4 different Curie temperatures are observed (Figure 4). Most of the samples have 3 Curie temperatures. Susceptibility vs temperature were measured on basalt powder in heating and cooling runs in the temperature range -200°C to 700°C . Polished thin sections were used in scanning electron microscope (SEM) and energy dispersive spectroscopy (EDS) for high-resolution element analysis. The precision of the analysis was supervised with magnetite, hematite and rutile standards. This is also observed in rock samples from the Reykjanes and Krafla geothermal areas (Dietze et al., 2010; Oliva-Urcia et al., 2011).

Multiple Curie temperatures can be explained by solid exsolution of titanomagnetite and/or low-temperature oxidation of titanomagnetite to form titanomaghemite. The Curie temperature of titanomagnetite depends on the ulvöspinel fraction. Based on laboratory studies on synthetic titanomagnetites, Lattard et al. (2006) established the relation

$$T_c^{TM} = -150u^2 - 580u + 851, \quad (21)$$

where u is the ulvöspinel fraction, and the Curie temperature T_c^{TM} is in Kelvin. Based on the data published by Moskowitz and Banerjee (1981), an empirical equation for the Curie temperature of titanomaghemite T_c^{TMGH} (Kelvin) can be expressed as (Figure 5)

$$T_c^{TMGH} = -110z^2 + 480z + 475, \quad (22)$$

where z is the degree of oxidation.

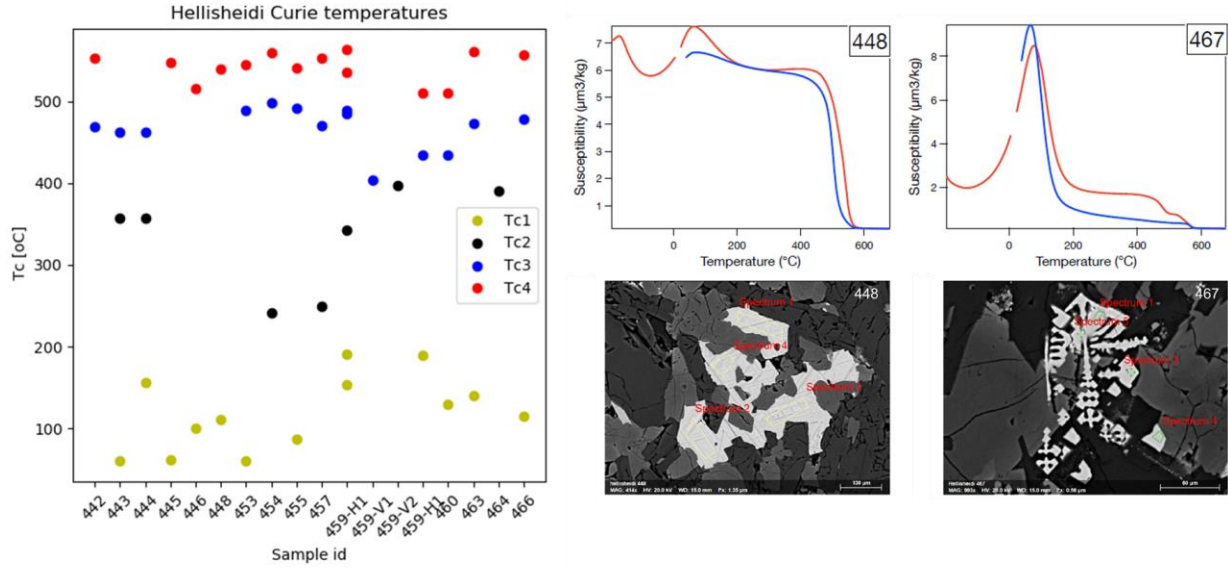


Figure 4: Magnetic measurements on rock samples from the Hellisheiði geothermal area on Iceland. Curie temperatures (left), temperature scan of magnetic susceptibility (upper right), and thin sections used in energy-dispersive X-ray spectroscopy (EDS) analysis (lower right). The Titanomagnetites are the lighter areas.

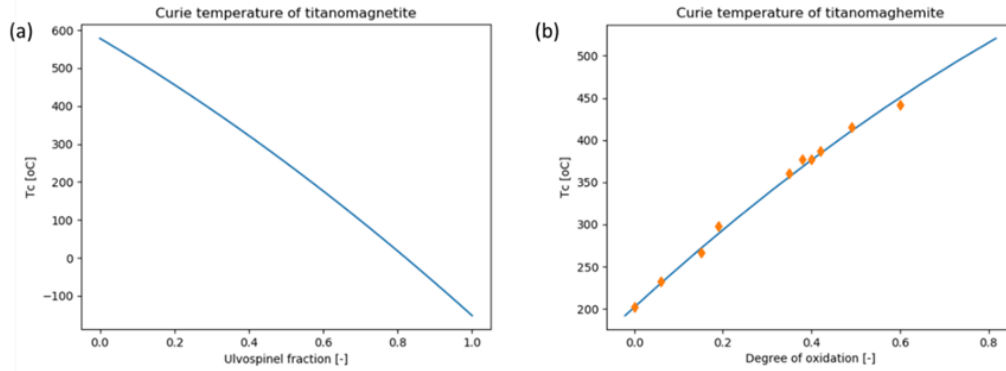


Figure 5: Curie temperature of titanomagnetite vs ulvöspinel fraction presented by Lattard et al., 2006 (left). Curie temperature of titanomaghemite vs degree of oxidation, based on data from Moskowitz and Banerjee (1981) shown as orange diamonds (right). The Curie temperatures are displayed in Celsius degrees.

On the microscopic level, magnetization can be explained as the effect of internal spin-spin interactions, and interactions between electron spin and an external magnetic field. To describe the thermal effects on magnetization, the one-dimensional Ising (1925) model from quantum statistics is used as a phenomenological model,

$$\frac{M}{M_0} = \tanh \left[\frac{T_C M}{T M_0} + \frac{C H}{T M_0} \right], \quad (23)$$

where M is the magnitude of the total magnetization vector (remanent and induced), M_0 is the magnetization at absolute zero, T is the temperature, T_C is the Curie temperature, and C is the Curie constant. The Ising model represents nearest-neighbor spin interactions. It captures both permanent

(remanent) and induced magnetization, and the transition to the paramagnetic domain near the Curie temperature. Linearization of the Ising model for high temperatures, leads to the well-known Curie-Weiss law. The Ising model can be used to represent the magnetic properties of a homogeneous single-domain magnetic phase. A heterogeneous mix of magnetic phases is approximated by a linear combination of single-phase models (Figure 6),

$$\tilde{M}(T) = \sum_j w_j M_j(T), \quad (24)$$

where w_j is the weight of phase j , and each of M_j are given by Equation 23. The linear superposition is supported by the magnetic potential being linear in magnetization.

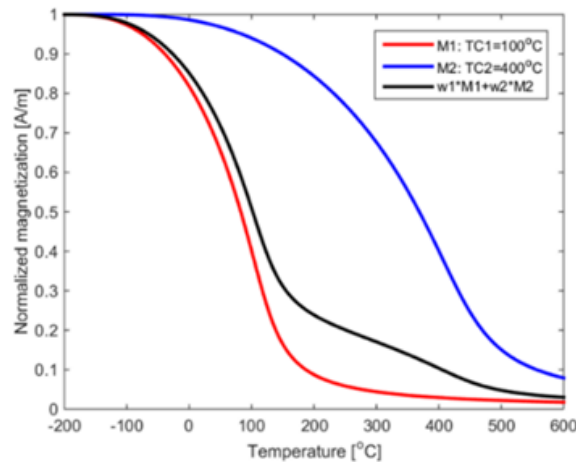


Figure 6: Two Ising models with different Curie temperatures $T_{C1} = 100$ °C (red) and $T_{C2} = 400$ °C (blue), and the superposition of the two models (black).

High-temperature, deuteric oxidation takes place right before and while basaltic rocks solidify, at temperature above 700°C , and hence above the Curie temperature of magnetite (~ 580 °C). Ilmenite (αFeTiO_3) lamellae are expelled, and consequently, the host titanomagnetite is enriched in magnetite. The ilmenite lamellae subdivide the initial titanomagnetite into smaller grains. Ilmenite is a paramagnetic mineral that does not contribute significantly to the magnetization.

Low-temperature oxidation of titanomagnetite occurs after solidification of the magma, typically at temperatures $T < 400$ °C. The main alteration process taking place is maghemitization due to fluid-rock interaction. Titanomaghemite belongs to the spinel group, but it is cation deficient since Fe^{2+} ions migrate out of the spinel lattice. It collapses to ilmenite when $T > 400$ °C (Ade-Hall et al., 1971).

The maghemitization of titanomagnetite takes place in two stages. First, a thin oxidized layer forms at the rim of the titanomagnetite grain. This process is relatively fast, and with relatively small activation energy E_1 . Gapeev and Gribov (1990) found experimentally the activation energies for varying initial ulvöspinel fractions and degrees of oxidation. For TM60 with low oxidation, the activation energy $E_1 \sim 145$ kJ/mole. Second, the oxidation progresses inwards, into the titanomagnetite grains by a slower diffusion process. This process was analyzed theoretically by

Fabian and Shcherbakov (2020), who suggested a linear increase in activation energy with increasing degree of oxidation,

$$E_2(z) = E_1 + \mu z, \quad (25)$$

where $\mu \sim 135$ kJ/mol is the gradient of the activation energy, and z is the degree of oxidation. For both oxidation stages, the reaction rate k_i is given by the Arrhenius equation,

$$k_i = A e^{-\frac{E_i}{RT}}, \quad (26)$$

where R is the gas constant, and $i = \{1, 2\}$.

To account for the two oxidation stages mentioned above, a mixed 1st and 2nd order kinetic model is proposed,

$$\frac{dx}{dt} = -\left(\frac{k_1 - k_2}{x_0}\right)x^2 - k_2x, \quad (27)$$

where k_1 and k_2 are the rate coefficients for the fast and slow oxidation stages, x_0 is the initial titanomagnetite fraction, and x is the time-dependent remaining volume fraction (concentration), of titanomagnetite. Equation 27 has the desired properties that the reaction rate is completely controlled by k_1 at $t = t_0$, $x = x_0$ (no oxidation) and by k_2 in the limit $t \rightarrow \infty$, $x \rightarrow 0$ (complete oxidation). For constant temperature, and hence constant rates k_1 and k_2 , the kinetic equation can be solved analytically (Figure 7),

$$x(t) = \frac{x_0 e^{-k_2 t}}{1 + \frac{k_1 - k_2}{k_2}(1 - e^{-k_2 t})}. \quad (28)$$

The constant-temperature solution, Equation 28, evaluated at each temperature of interest, is a good approximation to the time-dependent numerical solution for Equation 27.

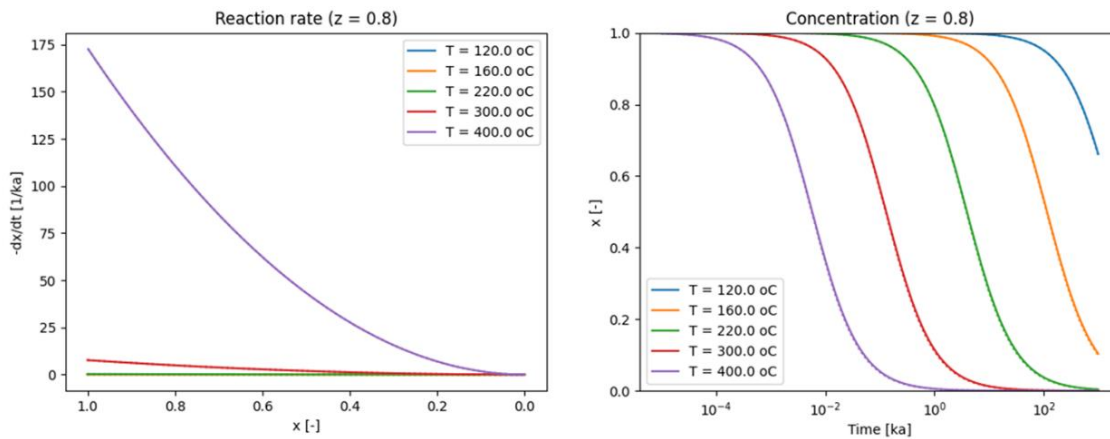


Figure 7: Mixed-order kinetic model for low temperature oxidation. Reaction rate vs remaining fraction of titanomagnetite (left). Titanomagnetite fraction vs geological time for selected temperatures. The solid line is the analytical solution in Equation 28, the dotted line shows the numerical solution to Equation 27 for comparison.

The reaction frequency A in the Arrhenius equation depends on the oxygen fugacity f_{O_2} . For a system under hydrostatic conditions, the oxygen fugacity is given by

$$\ln f_{O_2} = \int \frac{V_{O_2} dp}{R T}, \quad (29)$$

where $V_{O_2} = 32$ ml/mol is the partial molar volume of oxygen, which can be assumed to be approximately constant (Ludwig and Macdonald, 2005). Data presented by Orman and Crispin (2010) indicate that cation-diffusion rates in titanomagnetite is proportional to $f_{O_2}^{2/3}$. Therefore, to incorporate the effect of oxygen fugacity in the kinetic model, the reaction frequency is approximated as

$$A = A_0 \phi f_{O_2}^{2/3}, \quad (30)$$

where A_0 is a parameter subject to local calibration.

When igneous rocks form by crystallization of magma, titanomagnetite forms as a solid solution of ulvöspinel and magnetite with initial fractions u_0 and v_0 , respectively (Butler, 1992; Wise et al., 2011). As the rock cools further, titanomagnetite enters miscibility gap, where it becomes unstable. and decompose by spinodal decomposition, into two new phases with compositions u_1, v_1 and u_2, v_2 , respectively. The phases may continue to decompose by binodal decomposition, however, this relies on nucleation, associated with an activation energy, and is a much slower process (Yund and McAllister, 1969).

Hence, for young, fast-cooling lavas, spinodal decomposition is the most relevant mechanism (Smith, 1980). The spinodal decomposition is controlled by the Gibbs free energy G , which for a two-component solid solution consists of an enthalpy term and an entropy term (Miracle and Senkov, 2017),

$$G(u, v, T) = Wuv + k_B T [(1 + h)u \ln u + (1 - h)v \ln v], \quad (31)$$

where, u is the fraction of ulvöspinel and v is the fraction of magnetite, and $u + v = 1$.

The first and second derivatives of the Gibbs free energy with respect to ulvöspinel fraction u are obtained as

$$\frac{\partial G}{\partial u} = -W(u - v) + k_B T [(1 + h) \ln u - (1 - h) \ln v + 2h], \quad (32)$$

$$\frac{\partial^2 G}{\partial u^2} = -2W + k_B T \left[\frac{(1 + h)}{u} + \frac{(1 - h)}{v} \right]. \quad (33)$$

The spinodal decomposition takes place when $\frac{\partial^2 G}{\partial u^2} < 0$, and terminates at the spinodal equilibrium defined by $\frac{\partial^2 G}{\partial u^2} = 0$ (Yund and McAllister, 1969). The parameter h introduces an asymmetry in the spinode, in agreement with the experimental results of Wise et al. (2011). Equation 33 is a square

equation for u , with two roots u_1 and u_2 , representing two different phases with different magnetite and ulvöspinel fractions, and correspondingly, two different Curie temperatures, which can be computed from Equation 21 (Figure 8).

Further details of the solid-exsolution model have been presented by Hokstad et al. (2020).

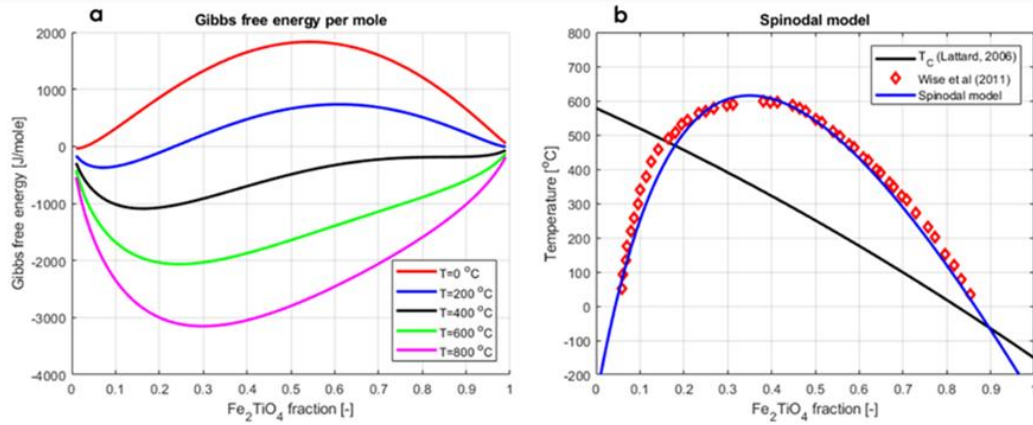


Figure 8: Gibbs free energy as function of ulvöspinel fraction for various temperatures (left). Model spinode (blue) calibrated to experimental results for titanomagnetite (red diamonds) presented by Wise et al. (2011) (right). Also shown is the Curie temperature of titanomagnetite (black) from Lattard et al. (2006).

With low-temperature oxidation and solid exsolution, three different Curie temperatures are obtained. Then, considering mass conservation and stoichiometric balancing, the weights for the Ising-model superposition in Equation 24 then become

$$w_1 = x \frac{u_0 - u_1}{u_2 - u_1}, \quad (34)$$

$$w_2 = x \frac{u_2 - u_0}{u_2 - u_1}, \quad (35)$$

$$w_3 = x_0 - x, \quad (36)$$

where the sum of the weights is $\sum w_i = x_0$, and x_0 is the initial fraction of titanomagnetite in the basalt (after high-temperature oxidation). Furthermore, u_0 is the fraction of ulvöspinel in the primary titanomagnetite ($u_0 = 0.6$ for TM60), and u_1 and u_2 are the ulvöspinel fractions in the two exsolution phases, respectively.

3. Synthetic model examples

3.1 Hengill-like model

To demonstrate Bayesian MGI, a synthetic-model example was created from a 3D subsurface temperature model of the Hengill geothermal area on Iceland, provided by the geothermal operator OR and Iceland GeoSurvey (ISOR). The model was based on well data with a maximum depth of approximately 3 km. For the present synthetic study, the model was extended to 7 km depth, with a temperature trend increasing with depth, and including a simulated magma chamber (Figure 9). A simple exponentially decaying trend was used for the porosity.

Geophysical models of resistivity, magnetization, density, P-wave velocity and S-wave velocity were computed using the rock-physics models presented above (Figure 10). Close-to fresh-water salinity was assumed for the electric resistivity modeling. A smectite cap, with clay-fraction $V_{cl} = 0.05$ within the basalt, was assumed for $T < 220$ °C, where smectite is stable.

The Bayesian inversion was then run, using all or a subset of the geophysical models as input. Inversion of log-resistivity, magnetization, density, P-wave velocity and v_p/v_s -ratio predict the posterior mean temperature accurately at all depths, and with a posterior variance of maximum ± 70 °C (Figure 11).

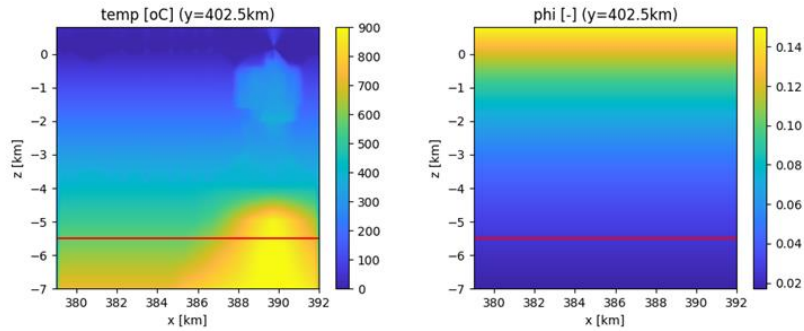


Figure 9: 3D temperature model from the Hengill area, west-to-east vertical section from the location of the Nesjavellir power plant (left), and porosity model (right).

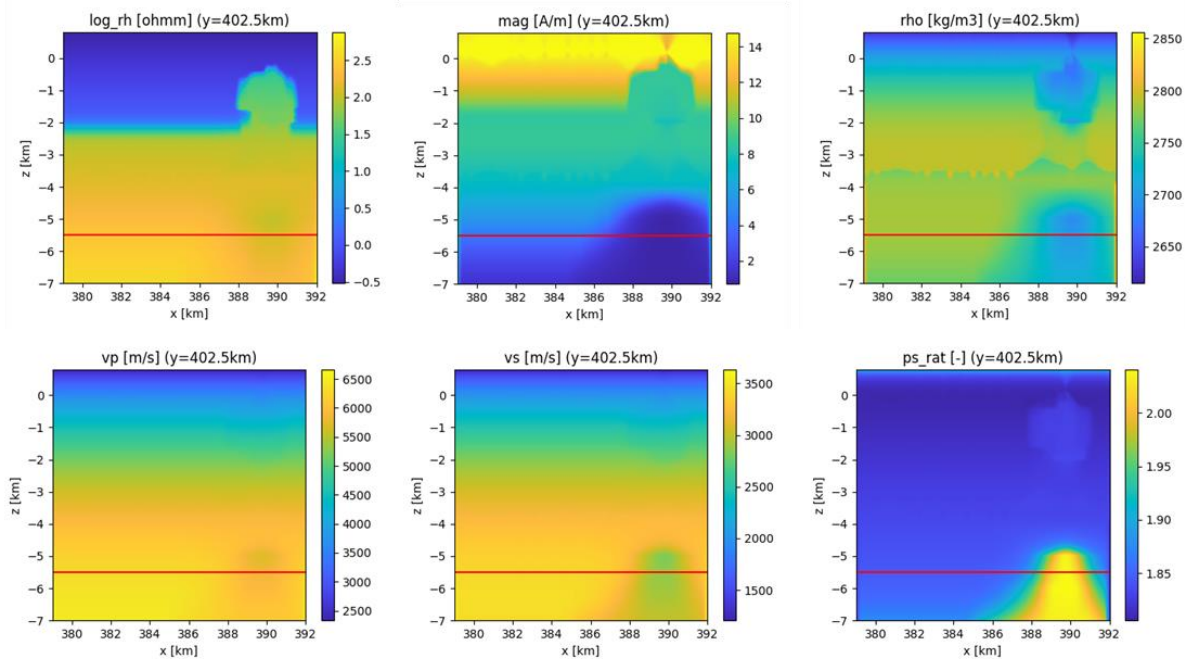


Figure 10: Simulated 3D geophysical models, computed using the rock-physics relations presented above, west-to-east vertical sections. From upper left to lower right: log10 resistivity, magnetization, density, P-wave velocity, S-wave velocity, and v_p/v_s -ratio.

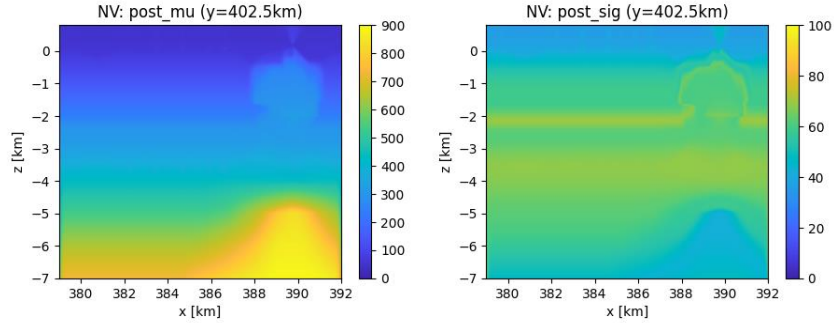


Figure 11: Inversion of 5 geophysical models; log-resistivity, magnetization, density, P-wave velocity and v_p/v_s -ratio. Posterior mean temperature (left), and posterior variance (right).

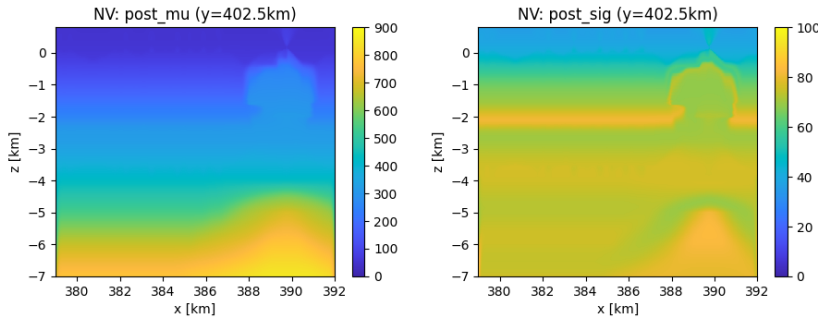


Figure 12: Inversion of 3 geophysical models; log-resistivity, magnetization, and v_p/v_s -ratio. Posterior mean temperature (left), and posterior variance (right).

Inversion of a subset of the geophysical models, log-resistivity, magnetization, density, P-wave velocity and v_p/v_s -ratio, still gives good prediction of the posterior mean temperature, however, the posterior variance increases significantly (Figure 12). This illustrates a general feature of MGI (and data integration in general); adding more types of consistent geophysical data and models leads to smaller uncertainty.

3.2 Bivariate multigeophysical inversion

Bivariate MGI, estimating both temperature and porosity, is demonstrated with a simple synthetic example. The input to the inversion was $\log_{10} R_h = 1.54 \Omega\text{m}$, $M = 8.5 \text{ A/m}$, $\rho = 2690 \text{ kg/m}^3$, $v_p = 4338 \text{ m/s}$, and $v_p/v_s = 1.82$. The posterior distribution in Equation 1 is the product of likelihood distributions, one for each geophysical model parameter, and the prior distribution. Visualizing the individual likelihood functions, in addition to the prior and posterior, demonstrates the sensitivity of each model parameter to temperature and porosity (Figure 13): Resistivity and density gives a trade-off between temperature and porosity, P-wave velocity is mainly sensitive to porosity, magnetization is only sensitive to temperature, and v_p/v_s -ratio is a good magma detector.

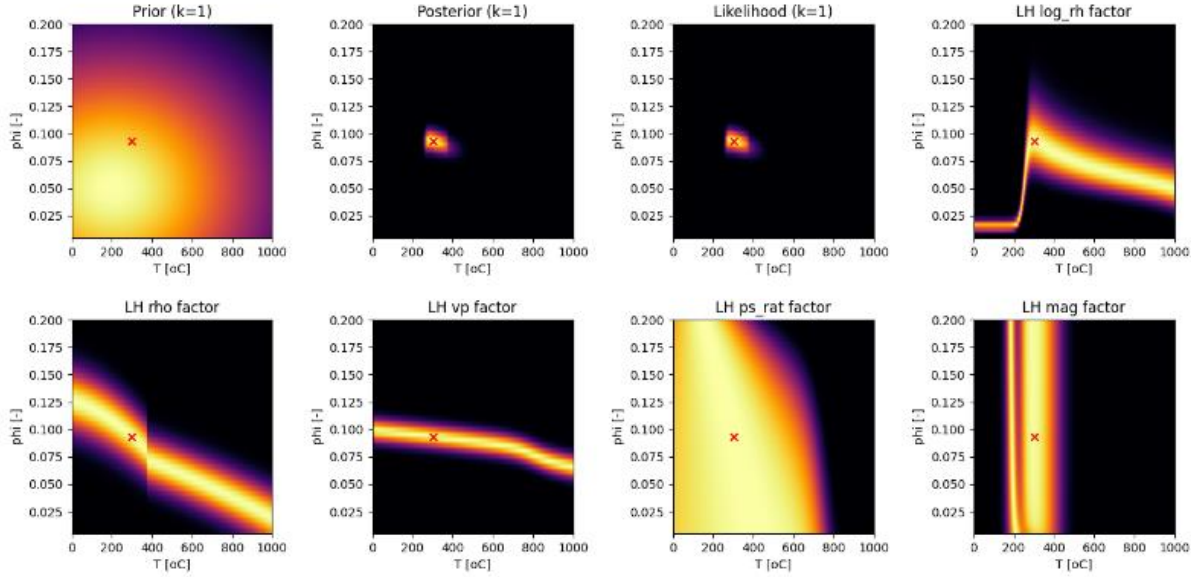


Figure 13: Posterior distribution and the individual likelihood-factors contributing to it. The axes of the plots are temperature and porosity, and the color indicates probability density; yellow is high probability, black is low probability. From upper left to lower right: prior distribution for temperature and porosity, posterior distribution, product of all likelihood distributions, and individual likelihoods of log resistivity, density, P-wave velocity, v_p/v_s -ratio and magnetization. The red cross indicates the true solution.

4. IDDP-3 exploration in the Hengill area

To contribute to exploration and siting of the IDDP-3 well, the proposed multigeophysical inversion method was applied to geophysical field data and models from the Hengill area. Data and models were shared by members of the DEEPEN project (Figure 14). Aeromagnetic data from OR was inverted, using the magnetic inversion scheme presented by Hokstad et al. (2020), to obtain a 3D magnetization model. A resistivity model from inversion of magnetotelluric (MT) data was provided by ISOR and OR (Benediktsdottir et al., 2021).

The inversion results indicate a zone with a deep heat source to the south of the Nesjavellir power plant at 2km depth below mean sea level (Figure 15), associated with anomalies of low resistivity and magnetization.. At 4km depth, the high-temperature zone is extending towards east, on the south side of the Nesjavellir plant. The posterior variances are low in areas where all geophysical models indicate the same temperature trend, and variances are high where models are contradictory. The high-temperature anomalies follow the main fault and fracture trend, with an orthogonal subtrend (Figure 16). Intrusions at depth of 4000m and more are of special interest for supercritical/superhot targets, since this increases the chance of obtaining high-enthalpy steam and efficient fluid flow (Scott et al., 2017).

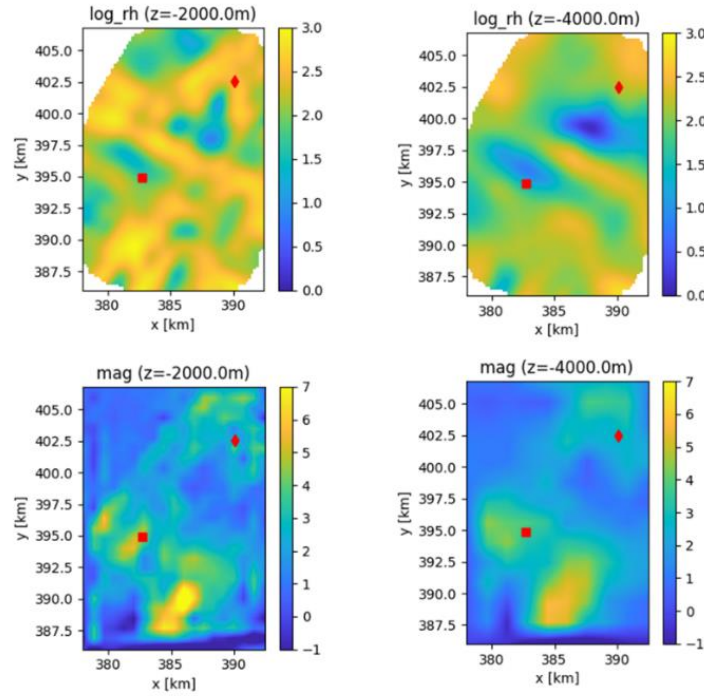


Figure 14: 3D geophysical models from the Hengill area. Horizontal sections of log₁₀ resistivity at -2000m and -4000m (top) and magnetization at -2000m and -4000m (bottom) relative to mean sea level. The red points indicate the locations of the Nesjavellir (diamond) and Hellisheiði (square) power plants.

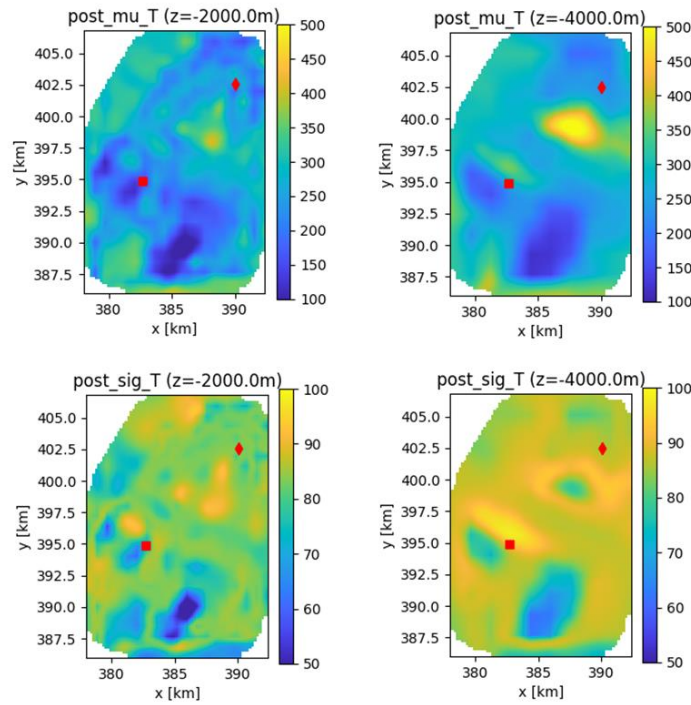


Figure 15: Results from multigeophysical inversion. Horizontal slices of posterior mean temperature at -2000m and -4000m (top), and posterior variance at -2000m and -4000m (bottom). The red points indicate the locations of the Nesjavellir (diamond) and Hellisheiði (square) power plants.

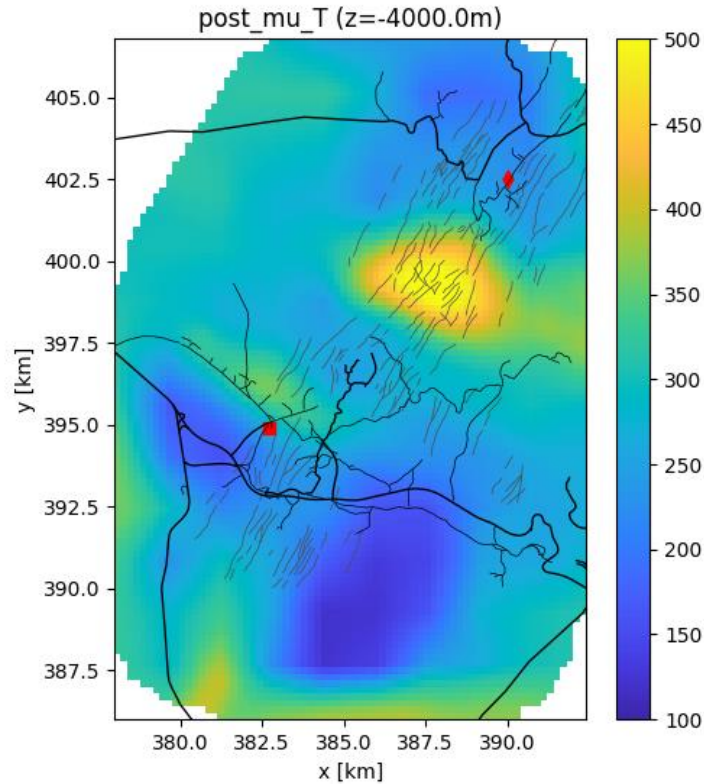


Figure 16: Results from multigeophysical inversion. Posterior mean temperature at -4000m relative to mean sea level. Grey lines show faults and fractures identified at the surface. The red points indicate the locations of the Nesjavellir (diamond) and Hellisheiði (square) power plants, and black lines show roads.

5. Discussion and conclusions

Multigeophysical inversion has previously been applied to various resource-exploration problems, including basin modeling, petroleum exploration, and mineral exploration. The topic addressed in the present work is geothermal exploration. The MGI method utilizes the framework of a naïve Bayes network, and conditional independence of different types of geophysical data. This again relies on independence of the noise in the various datasets.

The last stage of MGI, estimation of temperature and, eventually, porosity of geothermal systems, is effectively a rock physics inversion. Rock-physics forward models relating geophysical parameters, such as resistivity, magnetization, density and seismic P-wave and S-wave velocities, to temperature and porosity is needed as part of the inversion. The rock physics models require some local calibration to each case, similar to the applications of rock physics in e.g. petroleum-reservoir characterization. So far, the MGI method has been applied to basaltic geothermal systems, with focus on supercritical targets, as addressed within the IDDP research program conducted on Iceland.

If 3D models from single-domain geophysical inversions are available, MGI can predict 3D bivariate estimates of posterior mean and variance for temperature and porosity. Univariate estimates of either temperature or porosity can effectively be obtained by specifying a small prior

variance for one (or the other) variable. The MGI method can be applied as part of a 3D PFA workflow, contributing to the derisking of the heat source, recharge and producibility play elements.

In the present study, the MGI method is demonstrated on data from the Hengill geothermal area on Iceland, with the aim of supporting exploration and siting of the IDDP-3 well. The quality of the MGI results depends on both the calibration of the rock physics models to the local geological setting, and the quality of the models from single-domain inversions of geophysical data. Inversion of data and geophysical models from the Hengill is still work in progress at the time of writing (August 2023).

Acknowledgements

This work was partly funded by the Geothermica DEEPEN Project through the Research Council of Norway (Grant Agreement No 731117).

Magnetic laboratory measurements on the rock samples from Hellisheiði, Iceland, were done by Nathan Church and Geertje ter Maat, Department of Geoscience and Petroleum, Norwegian University of Science and Technology (NTNU), Trondheim.

We thank Asdis Benediksdóttir (OR), Vala Hjörleifsdóttir (OR), Kristján Óttar Klausen (ISOR), Amanda Kolker (NREL), Nicole Taverna (NREL), Patrick Dobson (LBNL), Pilar Sánchez-Pastor (ETH), Sin-Mei Wu (ETH), Anne Obermann (ETH), Tina Kaschwich (NORSAR), Carsten F. Sørli (Equinor), Jan Inge Tollefsrud (Equinor), Kenneth Duffaut (Equinor), Arild Buland (Equinor) and Jo Eidsvik (NTNU) for challenging discussions on the MGI methodology, Bayesian networks, and the rock-physics models used in the inversion.

We thank ISOR and OR for permission to use the MT resistivity model from the Hengill area, and OR for permission to use the aeromagnetic data.

We thank Equinor for permission to publish this work.

REFERENCES

- Ade-Hall, J.M., Palmer, H.C., and Hubbard, T.P., 1971, The magnetic and opaque petrological response of basalts to regional hydrothermal alteration: *Geophys. J. R. Astr. Soc.*, **24**, 137-174.
- Avset, P., and Lehoccki, I., 2021, 3D Subsurface Modeling of Multi-Scenario Rock Property and AVO Feasibility Cubes-An Integrated Workflow: *Frontiers in Earth Science*, **9**, doi: <https://doi.org/10.3389/feart.2021.642363>
- Bali, E., Aradi, L.E., Zierenberg, R.A, Diamond, L.A., Pettke, T., Szabo, A., Guðfinnsson, G.H., Friðleifsson, G.Ó., and Szabo, C., 2020, Geothermal energy and ore-forming potential of 600 °C mid-ocean-ridge hydrothermal fluids: *Geology*, **48**: 1221–1225
- Benediktsdóttir, Á., Árnason, K., Karlsdóttir, R., Vilhjálmsson, A. M., and Kristjánsson, B. R., 2021. Detailed resistivity models of sub-areas of the Hengill geothermal field, Iceland, in *Proceedings world geothermal congress*.

- Brace, W.F. and Orange, A.S., 1968, Electrical resistivity changes in saturated rocks during fracture and frictional sliding. *J. Geophys. Res.*, **73**, 1433-1445.
- Butler, R.F., 1992, *Paleomagnetism: Magnetic Domains to Geologic Terranes*. Blackwell Scientific Publications.
- Dietze, F., A. Kotny, I. Heyde, and C. Vahle, 2010, Magnetic anomalies and rock magnetism of basalts from Reykjanes (SW-Iceland): *Studia Geophysica et Geodaetica*, **55**, 109-130.
- Elders, W.A. Friðleifsson, G.Ó., Zierenberg, R.A., Pope, E.C., Mortensen, A.K., . Guðmundsson, Á , Lowenstern, J.B. , Marks, N.E., Owens, L., Bird, D.K., Reed, M., Olsen, N.J., and Schiffman, P., 2011, Origin of a rhyolite that intruded a geothermal well while drilling in a basaltic volcano, at Krafla, Iceland: *Geology*, **39**, 231-234.
- Eberhardt-Phillips, D., Han, D-H. and Zoback, M.D., 1989, Empirical relationships among seismic velocity, effective pressure, porosity and clay content: *Geophysics*, **54**, 82-89.
- Faulds, J.E., Craig, J.W., Hinz, N.H., Coolbaugh, M.F., Glen, J.M., Earney, T.E., Schermerhorn, W.D., Peacock , J., Deoreo, S.B., Siler , D.L., 2018, Discovery of a blind geothermal system in southern Gabbs Valley, western Nevada, through application of the play fairway analysis at multiple scales: *GRC Transactions* **42**.
- Friðleifsson, G.Ó., Elders, W.A., and Albertsson, A., 2014, The concept of the Iceland deep drilling project: *Geothermics*, **49**, 2-8.
- B. R. Hacker, G. A. Abers and S. M. Peacock, Subduction factory 1. Theoretical mineralogy, densities, seismic wave speeds, and H₂O contents, *Journal of Geophysical Research: Solid Earth*, **108**.
- Han, D-H., Nur, A., and Morgan, D., 1986, Effects of porosity and clay content on wave velocities in sandstones: *Geophysics*, **51**, 2093–2107.
- Gapeev, A.K., and Gribov, S.K., 1990, Kinetics of single-phase oxidation of titanomagnetite: *Physics of the Earth and Planetary Interiors*, **63**, 58-65.
- Hjörleifsdóttir, V., Kolker, Sørle, C., Hokstad, K., Stefánsson, A., Goertz-Allman, B., Dobson, P., Sonnenthal, E., Benediktsdóttir, A., Guðnason, E.A., Dahm, T., Obermann, A., Souque, C., 2023, DERisking Exploration for geothermal Plays in magmatic Environments – Results and Perspectives from the DEEPEN Project. *GRC Transactions* **47** (this volume).
- Hokstad, K., Tašárová, Z.A., Clark, S.A., Kyrkjebø, R., Duffaut, K., Fichler, C. & Wiik, T. 2017, Radiogenic heat production in the crust from inversion of gravity and magnetic data: *Norwegian J. of Geology* **97**, 241–254. <https://dx.doi.org/10.17850/njg97-3-04>.
- Hokstad, K., and Tānavsuu-Milkeviciene, K., 2017: Temperature prediction by multigeophysical inversion: Application to the IDDP-2 well at Reykjanes, Iceland. *GRC Transactions* **42**, 1141-1152.
- Hokstad, K., Alasonati-Tašárová, Z., Sæther, B.M., and Tānavsuu-Milkeviciene, K., 2020, Inversion of Magnetic Data for Subsurface Temperature: *Proceedings World Geothermal Congress 2020+1*.
- Hokstad, 2020: Method of estimating mineral content of a geological structure: Patent Application WO 2020/222652

- Hokstad, K., 2022, Method of estimating polymetallic nodule abundance: Patent Application WO 2022/093036 A1.
- Ising, E., 1925, Beitrag zur theorie des ferromagnetismus: *Z.Phys*, **31**, 253-258.
- Kern, H., Gao, S., and Liu, Q-S., 1996: Seismic properties and densities of middle and lower crustal rocks along the North China Geoscience Transect. *Earth and Planetary Science Letters*, **139**, 439-455.
- Kolker, A.; Taverna, N.; Dobson, P.; Benediksdóttir, A.; Warren, I.; Pauling, H.; Sonnenthal, E.; Hjörleifsdóttir, V.; Hokstad, K.; Caliendo, N., 2022, Exploring for Superhot Geothermal Targets in Magmatic Settings: Developing a Methodology: *GRC Transactions* **46**.
- Lattard, D., R. Engelmann, A. Kontny, and U. Sauerzapf, 2006, Curie temperatures of synthetic titanomagnetites in the Fe-Ti-O system: Effects of composition, crystal chemistry, and thermomagnetic methods: *J. Geophys. Res.*, **111**.
- Ludwig H., and Macdonald, A.G., 2005, The significance of the activity of dissolved oxygen, and other gases, enhanced by high hydrostatic pressure: *Comp. Biochem. and Physiology, Part A*, **140**, 387-395. doi:10.1016/j.cbpb.2005.02.001
- Mavko, G., Mukerji, T., and Dvorkin, J., 2009: *The Rock Physics Handbook*, 2nd Edition: Cambridge University Press.
- Miotti, F.M., Golfre Andreasi, F., Brambilla, C., Re, S., Wiik, T., and Hokstad, K., 2020, Deterministic and Statistical Workflows for Multigeophysical Reservoir Characterization: 82nd EAGE Conference and Exhibition, Expanded Abstracts.
- Miracle, D., and O. Senkov, 2017, A critical review of high entropy alloys and related concepts: *Acta Materialia*, **122**, 448-511.
- Moskowitz, B.M., and Banerjee, S.K., 1981, A Comparison of the Magnetic Properties of Synthetic Titanomagnetites and Some Oceanic Basalts: *J. Geophys. Res.*, **86**, 11869-11882.
- Mostafa, M.S., Afify, N., Gaber, A., and Abozid E.F., 2003. Electrical Resistivity of Some Basalt and Granite Samples from Egypt: *Egypt. J. Sol.*, **26**, 25-32
- Okamoto, K., Asanuma, H., Ishibashi, T., Yamaya, Y., Saishu, H., Yanagisawa, N., Ishisuka, K., Fujimitsu, Y., Kitamura, K., Kajiwar, T., Horimoto, S., Shimada, K., 2019, Geological and engineering features of developing ultra-high-temperature geothermal systems in the world: *Geothermics*, **82**, 267-281.
- Oliva-Urcia, B., Kontny, A., Vahle, C., and Schleicher, A.M., 2011, Modification of the magnetic mineralogy in basalts due to fluid–rock interactions in a high-temperature geothermal system (Krafla, Iceland). *Geophys. J. Int.*, **186**, 155-174.
- Prevot, M, Lecaille, A., and Mankinen, E.A., 1981, Magnetic effects of magnetization of oceanic crust: *J. Geophys. Res.*, **86**, 4009-4020.
- Sen, P. and Goode, P.A, 1992: Influence of temperature on electrical conductivity on shaly sands: *Geophysics*, **57**, 89-96.
- Scott, S., Driesner, T., and Weis, P., 2017, Boiling and condensation of saline geothermal fluids above magmatic intrusions, *Geophys. Res. Lett.*, **44**, 1696–1705, doi:10.1002/2016GL071891

- Smith, P., 1980, Spinodal decomposition in a titanomagnetite: *American Mineralogist*, **65**, 1038-1043
- Usher, G., Harvey, C., Johnstone, R., and Anderson, E., 2000. Understanding the Resistivities Observed in Geothermal Systems: *Proc. World Geothermal Congress*.
- Van Orman, J.A., and Crispin, K.I., 2010, Diffusion in Oxides: *Reviews in Mineralogy & Geochemistry*, **77**, 757-825.
- Yund, R., and R. McAllister, 1969, Kinetics and mechanisms of exsolution: *Chemical Geology*, **6**, 5-30.